

LETTER

Dual-wavelength single-longitudinal-mode sub-ns lasers with high pulse repetition frequency

To cite this article: Zheng Song *et al* 2023 *Laser Phys. Lett.* **20** 015001

View the [article online](#) for updates and enhancements.

You may also like

- [Areas under peripheral pulse waves: a potential marker of atherosclerotic changes](#)
Mikko Peltokangas, Jarmo Verho, Ville M Mattila *et al.*
- [Effect of heat-induced pain stimuli on pulse transit time and pulse wave amplitude in healthy volunteers](#)
Marit H N van Velzen, Arjo J Loeve, Minke C Kortekaas *et al.*
- [Combining orbit jump and potential wells optimizations for nonlinear vibration energy harvesters](#)
C Saint-Martin, A Morel, L Charleux *et al.*

Letter

Dual-wavelength single-longitudinal-mode sub-ns lasers with high pulse repetition frequency

Zheng Song¹, Yuanji Li^{1,2,*}, Zeru Yu¹, Jinxia Feng^{1,2} and Kuanshou Zhang^{1,2,*}¹ State Key Laboratory of Quantum Optics and Quantum Optics Devices, Institute of Opto-Electronics, Shanxi University, Taiyuan 030006, People's Republic of China² Collaborative Innovation Center of extreme Optics, Shanxi University, Taiyuan 030006, People's Republic of ChinaE-mail: liyuanji@sxu.edu.cn and kuanshou@sxu.edu.cn

Received 25 August 2022

Accepted for publication 6 December 2022

Published 21 December 2022

**Abstract**

A theoretical model suitable to the dual-wavelength electro-optical Q-switched laser was established. Based on the optimizations on the time-varying Q-switched loss, doped concentration of the gain medium, and transmission of the output coupler, 1 kHz 1064 nm and 532 nm single-longitudinal-mode pulse lasers both with sub-nanosecond pulse width (PW) were obtained. The measured PWs of the dual-wavelength lasers agreed well with the theoretical predictions. At a pump energy of 3.7 mJ, the PWs of the 1064 nm and 532 nm lasers were 0.97 ns and 0.61 ns, the single pulse energy of the two lasers were 0.55 mJ and 0.29 mJ. The beam quality factor, the energy fluctuation and the time jitter of the 1064 nm laser were 1.58, 0.000063% and 2.18 ps; and that of the 532 nm laser were 1.35, 0.000011% and 1.56 ps.

Keywords: rate equation model, dual-wavelength, sub-nanosecond, low fluctuations and jitter

(Some figures may appear in colour only in the online journal)

1. Introduction

Robust dual-wavelength pulse lasers with high pulse repetition frequency (PRF) are highly desired in either medical and outdoor detection applications [1–3] or laser precision machining [4, 5]. Particularly, to meet the need of high speed high resolution photoacoustic microscopy (PAM) for living animals [6–8], dual-wavelength laser operation with relative large wavelength separation is necessary for improving the imaging contrast and expand the usage scenario of the PAM, the laser pulse width (PW) should be narrowed to sub-nanosecond (ns) level to get a minimum resolvable scale of

the PAM less than 1.5 μm , and the fluctuations of both the laser PW and the single pulse energy (SPE) should be as low as possible at the same time since the image of PAM is obtained using the data got from tens of thousands of single point measurements [9–11].

However, the majority of the high PRF Q-switched lasers without excess amplifier presented in the previous investigations can not possess sub-ns PW, several hundred microjoule (μJ) SPE and good stability simultaneously. For instance, Zayhowski and Dill narrowed the PW of the 1 kHz PRF electro-optical (EO) Q-switched laser to picosecond (ps) level by reducing the cavity length, but the laser SPE was only 12 μJ [12]. Zhou *et al* demonstrated a 1 kHz passive Q-switched laser with a PW of 0.49 ns, but the fluctuation of the laser SPE was as high as 5.4% during a period of 1 s [13].

* Authors to whom any correspondence should be addressed.

Li *et al* demonstrated a laser with a PRF of 2 kHz and a SPE of 0.75 mJ using a combination of EO Q-switch and passive Q-switch, but the laser PW was 2.5 ns that beyond the sub-ns level [14].

To date, extra-cavity single-pass second harmonic generator (SHG) was the most popular device to get dual-wavelength laser operation. However, high quality dichroic mirror or polarization prism were needed for separating the fundamental (FD) wave and second harmonic (SH) wave. More importantly, the beam quality of the residual FD wave passing through the SHG always became worse since there existed a space-dependent nonlinear loss.

In this letter, a theoretical model for dual-wavelength pulse lasers was established. The FD laser was intrinsically divided to be two parts by controlling the time-varying EO Q-switched loss. The time-varying EO Q-switched loss, the doped concentration of the gain medium and the output coupling transmission were optimized to get robust dual-wavelength pulse lasers with high PRF and sub-ns PW.

2. Theoretical analysis of the 1064 nm and 532 nm dual wavelength pulsed laser

2.1. Rate equations model

For an EO Q-switched laser, the rate equations can be written as

$$dn/dt = -\gamma n c \sigma_{se} \phi, \quad (1)$$

$$d\phi/dt = [2n\sigma_{se}\phi l - \phi(\delta_0 + \delta_{QS} + T_{oc})][c/(2l_c)], \quad (2)$$

with the initial conditions of

$$n_0 = \frac{P_{in}\tau_f(1 - \exp(-\alpha l))}{h\nu_p} \left[1 - \exp\left(-\frac{T_p}{\tau_f}\right) \right] \frac{\omega_l^2}{\pi\omega_{pa}^4 l}, \quad (3)$$

$$\phi_0 = n_0 \frac{l}{c\tau_f} \frac{d\Omega}{4\pi}, \quad (4)$$

and the time dependent loss of EO Q-switch (δ_{QS}) of:

$$\delta_{QS}(t) = \cos^2 \left(\frac{\pi}{2} \frac{V_{hl}}{V_{\lambda/4}} \left(1 - \exp \left[- \left(\frac{t}{t_{qr}} \right)^4 \right] \right) \right)^4 \times \exp \left[- \left(\frac{t - t_{qs}/2}{t_{qs}} \right)^{400} \right], \quad (5)$$

where the spectroscopic parameters including the stimulated emission cross-section of gain medium at the laser wavelength (σ_{se}), absorption coefficient of gain medium at the pump wavelength (α) and fluorescence lifetime of gain medium (τ_f) are all depending on the doped concentration of the gain medium (D_c). In the case of 808 nm laser pumped Nd:YVO₄ laser operating at 1064 nm, the relations between the three

Table 1. Parameters and typical values.

| Symbol | Physical meaning | Typical value |
|-----------------|--|-----------------------------------|
| n | Population inversion density | — |
| ϕ | Photon density | — |
| γ | Inversion reduction factor | 0.66 |
| c | Light speed in vacuum | 3×10^8 m s ⁻¹ |
| l | Length of the gain medium | 8 mm |
| l_c | Effective laser cavity length | 81.3 mm |
| T_{oc} | Transmission of output coupler | 30% |
| δ_0 | Dissipative loss | 1% |
| δ_{QS} | Loss caused by Q-switch | — |
| P_{in} | Incident pump power | 25 W |
| T_p | Pump pulse width | 150 μ s |
| $h\nu_p$ | Energy of pump photon | 2.46×10^{-19} J |
| ω_{pa} | Average beam radii of pump beam inside the laser crystal | 300 μ m |
| ω_l | Average beam radii of laser beam inside the laser crystal | 245 μ m |
| $d\Omega$ | Solid angle of spontaneous emission that makes contribution to the stimulated emission | 1 mrad |
| V_{hl} | High-level voltage of the driving signal sent to PC | 690 V |
| $V_{\lambda/4}$ | Quarter wave voltage of PC | — |
| t_{qr} | Rise time of the driving signal | 4 ns |
| t_{qs} | A constant determined by the duration of $V(t) = V_{hl}$ | 160 ns |

parameters and D_c (with an unit of at.%) can be written as [15–17]:

$$\sigma_{se} = \left(\begin{array}{l} 8.36075 + 2221.49 * D_c \\ -102818.3 * D_c^2 - 1490820 * D_c^3 \end{array} \right) * 10^{-23}, \quad (6)$$

$$\alpha = (13.5 * D_c + 0.8) * 100, \quad (7)$$

$$\tau_f = (-1650 * D_c + 106.67) * 10^{-6}, \quad (8)$$

Besides that, the definitions of the other symbols mentioned above and their typical values are given in table 1.

Considering the case that the extra-cavity SHG was based on a type-I phase matched LBO crystal with a double refraction angle of 0, supposing that the absorption of the LBO

Table 2. SHG parameters and typical values.

| Symbol | Physical meaning | Typical value |
|------------------|--|-----------------------------------|
| A | Effective area of the FD wave inside the LBO crystal | $7.068 \times 10^4 \mu\text{m}^2$ |
| l_{LBO} | Length of LBO crystal | 20 mm |
| d_{eff} | Effective nonlinear coefficient of SHG | 1.16 pm V^{-1} |
| n_0 | Refractive index of the FD wave in the LBO crystal | 1.6055 |
| ϵ_0 | Permittivity of vacuum | 8.85×10^{-12} |
| λ_0 | Wavelength of the FD wave | 1064 nm |
| D_c | Doped concentration of the gain medium | 0.7 at. % |

crystal at the wavelengths of FD wave and SH wave can be neglected, and the SHG is in perfect phase matching, the power of the harmonic wave can be written as [18]:

$$P_{\text{SHG}} = \tanh^2 \left[\kappa l_{\text{LBO}} \left(\frac{P_0}{A} \right)^{\frac{1}{2}} \right] P_0, \quad (9)$$

$$\kappa = \frac{8\pi d_{\text{eff}}}{\lambda_0 n_0}, \quad (10)$$

where the definitions of the symbols mentioned in equations (6)–(10) and their typical values are given in table 2.

In this study, the power of the FD wave emitted from the output coupler (OC) (FD1) is indicated by P_1 . The other FD wave (FD2) was emitted from the polarizer acting as a varying-reflection mirror, its power, also the power of the FD wave at the front face of LBO crystal is indicated by P_0 .

Using equations (1)–(10) and the parameter values given in tables 1 and 2, the dependences of the normalized intensities of FD1, FD2 and SH lasers on time (t) at different values of V_{hl} were simulated and shown in figure 1. It can be seen, when $V_{\text{hl}} = V_{\lambda/4}$, there only exists FD1 wave which has a relative long falling edge, and the laser PW is 1.6 ns. When V_{hl} is raised up to $1.4^*V_{\lambda/4}$, the falling edge of the FD1 laser pulse becomes steeper, for the reason that the photons circulated in the cavity after giant pulse emission can be blocked owing to the fast varied intracavity loss during the change of V_{hl} from $V_{\lambda/4}$ to $1.4^*V_{\lambda/4}$. In this case, FD2 and SH waves can be obtained owing to the partly opened Q-switch, and the PWs of the FD1, FD2 and SH waves become 1.1 ns, 1.1 ns and 0.79 ns. However, in the case of $V_{\text{hl}} = 1.8^*V_{\lambda/4}$, the PW of the three beams are 1.3 ns, 1.3 ns and 0.93 ns, which are no longer narrower due to a large intracavity loss during the pulse generation process. Note that the PWs of FD1 and FD2 are always the same, but there is a time delay of 0.15 ns between the two beams corresponding to the transit time of photons from the OC to the polarizer. Note also that the symmetry of the line

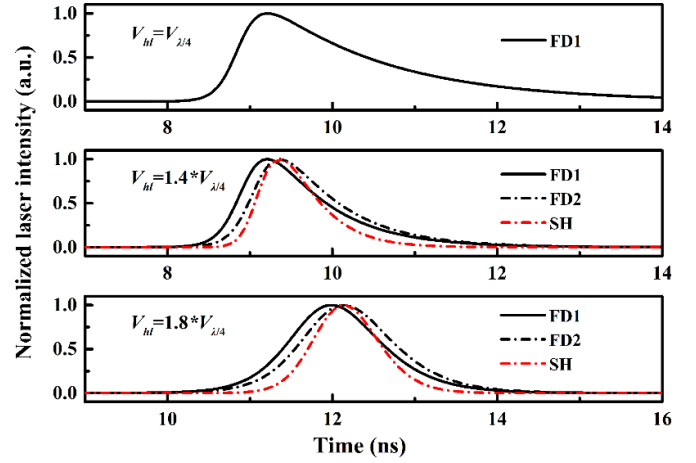


Figure 1. Single pulse shapes of the fundamental wave and harmonic wave at different V_{hl} : (a) $V_{\text{hl}} = V_{\lambda/4}$, (b) $V_{\text{hl}} = 1.4^*V_{\lambda/4}$, (c) $V_{\text{hl}} = 1.8^*V_{\lambda/4}$.

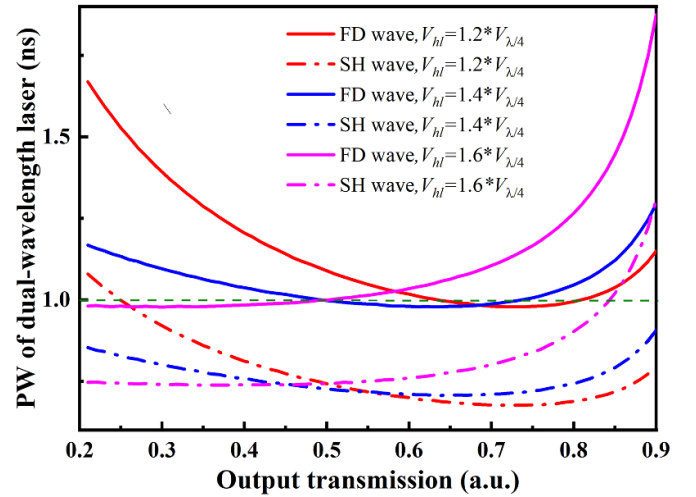


Figure 2. Evolution of the PWs of both the FD and SH waves with varying output coupling transmission at different V_{hl} .

shape of the laser pulse was modified along with the change of V_{hl} , as well as the SH generation process.

From equations (2) to (6)–(8), one may notice that T_{oc} and D_c are both key parameters that affect the PW and SPE of the dual-wavelength Q-switched lasers. Figures 2 and 3 shows the evolution of the PWs and SPEs of FD1 and SH waves with varying output coupling transmission at different V_{hl} . It can be seen, there is a T_{oc} enabling the narrowest PWs of the two waves, which are 75.7%, 72%, 62.5% and 34% for $V_{\text{hl}} = V_{\lambda/4}$, $V_{\text{hl}} = 1.2^*V_{\lambda/4}$, $V_{\text{hl}} = 1.4^*V_{\lambda/4}$, and $V_{\text{hl}} = 1.6^*V_{\lambda/4}$, respectively. Since the dual-wavelength pulse lasers are used as the excitation source of PAM, firstly, the PWs of both FD and SH waves should be below 1 ns to achieve a minimum resolvable scale of $1.5 \mu\text{m}$, which is half of the typical scale of blood capillary; secondly, for dual-wavelength PAM, the imaging depth depends on two factors, one is the lower one of the SPEs of FD1 and SH waves which set a lower limit of imaging depth, the other is

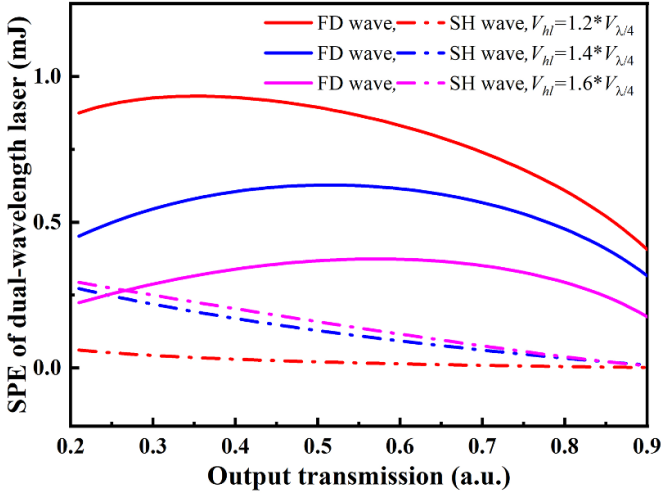


Figure 3. Evolution of the SPEs of both the FD and SH waves with varying output coupling transmission at different V_{hl} .

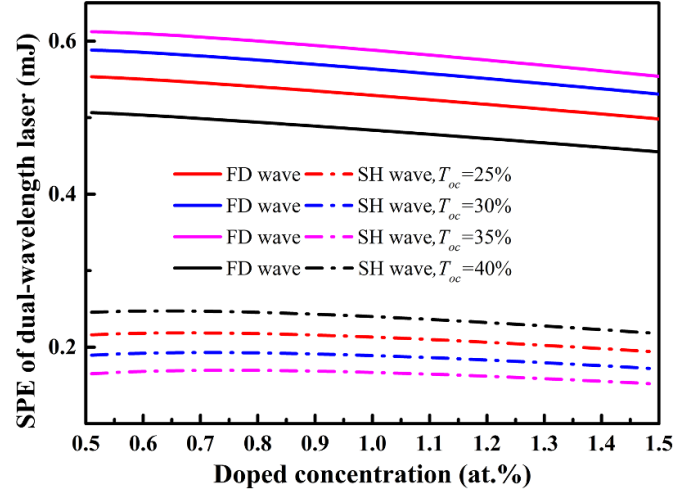


Figure 5. Evolution of the SPEs of both FD1 and SH waves with varying D_c at different T_{oc} .

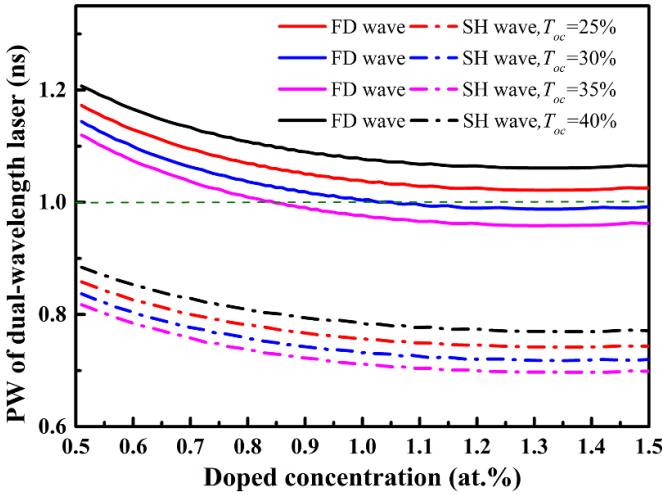


Figure 4. Evolution of the PWs of both FD1 and SH waves with varying D_c at different T_{oc} .

the higher one of the SPEs of FD and SH waves, since the Grueneisen parameter of the image object can be raised up, and consequently improve the PAM signals, by high power laser heating [19]. Hence a parameter can be defined to weigh the optimum laser SPE combination: $SR = SPE_{FD} * SPE_{SH}$. The optimization was gradually accomplished and the procedure in this step was based on a screening conditions of $PW_{FD1} \& PW_{SH} < 1.1$ ns and $SR > 0.1$, then the best value of $V_{hl} = 1.4 * V_{\lambda/4}$ and prefer range of output transmission (from 30% to 40%) can be obtained.

In the second step of optimization, the evolutions of the PWs and SPEs of FD1 and SH waves with varying D_c at different T_{oc} were simulated at the case of $V_{hl} = 1.4 * V_{\lambda/4}$. As shown in figures 4 and 5. Using the final criteria that $PW_{FD1} \& PW_{SH} < 1$ ns and $SR > 0.11$, the optimum values of doped concentration (1 at.%) and output transmission (30%)

can be determined, in which case sub-ns dual-wavelength lasers with sufficient high SPEs can be obtained.

3. Experimental setup and results

The experimental setup of the Q-switched 532 nm and 1064 nm laser was schematically shown in figure 6. The setup was mainly consisted with two parts, namely the cavity of Q-switched fundamental laser and the single-pass LBO-based SHG device. In the Q-switched laser cavity, an *a*-cut YVO_4 -Nd:YVO₄ composite crystal with a dimension of $3 \times 3 \times (2 + 8)$ mm³ and a doping concentration of 1 at.% was employed as gain medium for balancing the need of short cavity length, high pump absorption, and thermal effect as weak as possible. Correspondingly, an 808 nm laser was injected into the gain medium for providing pump energy after passing through a volume Bragg grating (VBG) with a transmissivity higher than 93% at 808 nm. Since the VBG also has a diffraction efficiency at 1064 nm exceeding 99.5%, a wavelength acceptance bandwidth of 0.3 nm and an angular selectivity of ± 2.4 mrad, the VBG not only played the role of input coupler, but also helped the selections of single-longitudinal-mode and TEM₀₀ transverse mode. Using a combination of a quarter-wave plate (QWP) and a dual-RTP-crystal based Pockels cell (PC), the Q-value of the laser cavity can be switched and the time-varying intracavity loss can be manipulated by tuning the high-level voltage of the Q-switch driver. Note that the Q-switched laser cavity has two export, while the OC with a curvature radius of 1000 mm and partial reflection coating at 1064 nm ($T_{1064 \text{ nm}} = 30\%$) was used to couple the *s*-polarized laser out from the cavity, and the 45° thin film polarizer with polarization distinction ratio higher than 1000:1 was employed for coupling the *p*-polarized laser out from the cavity, as well as for further improving the purities of the polarization and longitudinal-mode

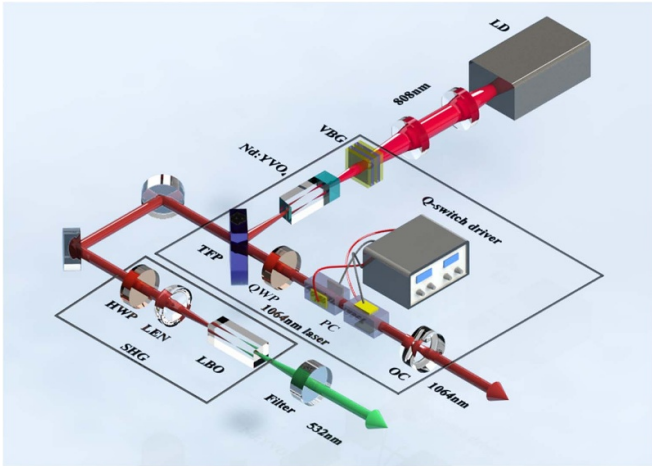


Figure 6. Schematic of the experimental setup.

of the 1064 nm laser. In the single-pass SHG device, a LBO crystal (cut at $\theta = 90^\circ$, $\phi = 0^\circ$) with a dimension of $3 \times 3 \times 20 \text{ mm}^3$ was used to achieve Type-I phase matched SHG.

For reducing the thermal effect, the pump laser was operated in quasi-continuous mode with a repetition frequency of 1 kHz and a duty cycle of 15%. Figure 7 shows the measured laser PW as a function of pump energy, in which the black and red data points indicate the measured PW of the FD1 laser and SH laser at $V_{\text{hl}} = 1.4 * V_{\lambda/4}$, the blue data points indicate the measured PW of the FD1 laser at $V_{\text{hl}} = V_{\lambda/4}$, and the black, red and blue curves indicate the corresponding theoretical predictions. Obviously, the experimental data agree well with the theoretical predictions. When the pump energy was increased from 1.6 mJ to 3.7 mJ, the PWs of the three lasers were all reduced monotonously. When the pump energy was 3.7 mJ, the PW of FD1 and SH lasers at $V_{\text{hl}} = 1.4 * V_{\lambda/4}$ were 0.97 ns and 0.61 ns, while the PW of FD1 at $V_{\text{hl}} = V_{\lambda/4}$ was 1.3 ns. Moreover, the SPEs of FD1 and SH lasers at $V_{\text{hl}} = 1.4 * V_{\lambda/4}$ were all monotonously increased, and the maximum energies of the two lasers were respectively 0.55 mJ and 0.29 mJ, which also coincided with the theoretical predictions.

More information of the laser output characteristics under a pump energy of 3.7 mJ when $V_{\text{hl}} = 1.4 * V_{\lambda/4}$ can be found in figures 8 and 9. In figures 8(a) and (b), the data points and curves respectively indicate the beam qualities of FD1 and SH lasers measured using a laser beam analyser (Spricon, Model: M2-200-BB; CCD: GRAS-20S4M-C). The measured beam qualities of the FD1 laser were $M_x^2 = 1.58$ along the horizontal direction and $M_y^2 = 1.31$ along the vertical direction. The measured beam qualities of the SH laser were $M_x^2 = 1.35$ along the horizontal direction and $M_y^2 = 1.12$ along the vertical direction. Figures 9(a) and (b) show the longitudinal mode structures of the FD1 and SH lasers measured using two etalons (thickness: 25 mm, coating: R@1064 nm&532 nm = $70\% \pm 1\%$). The measured interference fringes indicate that both the FD1 and SH lasers were in single-longitudinal-mode operation.

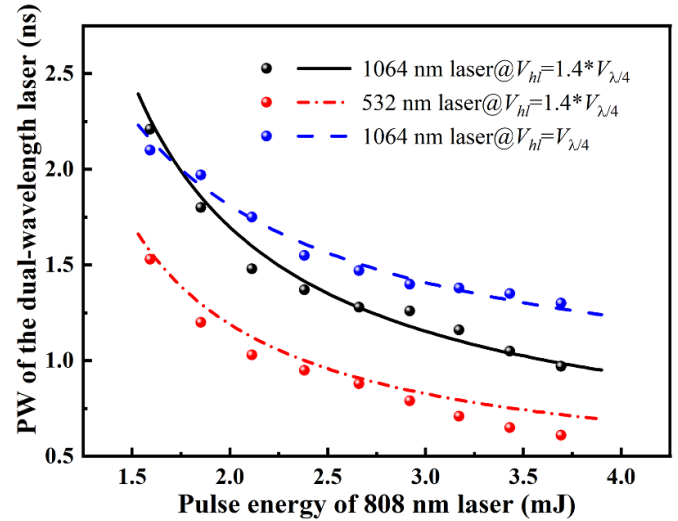


Figure 7. Measured PWs of the FD1 and SH lasers with varying pump energy.

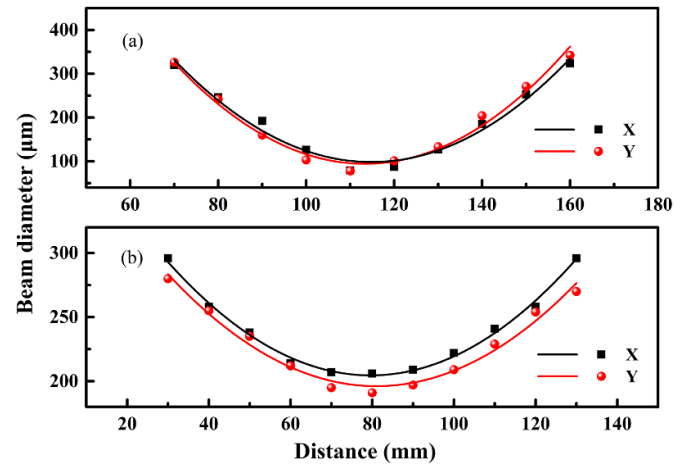


Figure 8. Measured beam quality of the FD1 (a) and SH (b) lasers.

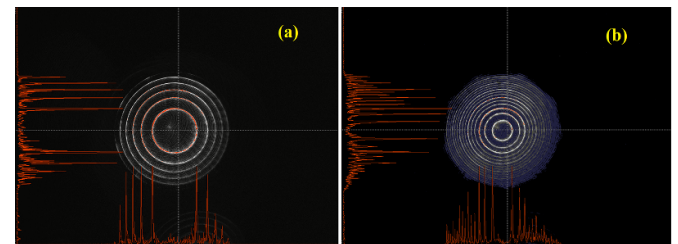


Figure 9. Measured longitudinal mode structures of the FD1 (a) and SH (b) lasers.

Laser noise was another key factor affect the imaging quality of PAM, where the energy fluctuation of the excitation laser induced the thermal noise of the imaged object, the jitter lower the signal-to-noise ratio of PAM. The noise characteristics of the dual-wavelength pulse lasers were measured by spectrum analysis method [20–22]. Figure 10 shows the single-side noise power spectra of the FD1 and SH lasers

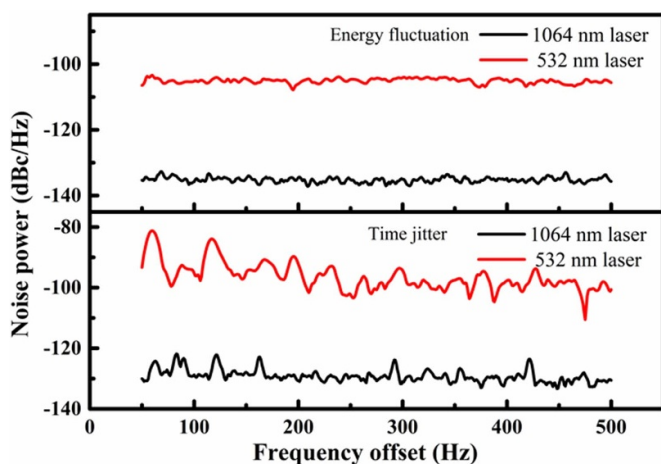


Figure 10. Single-side noise power spectra of the FD1 and SH lasers.

when the average power of the pulse train incident onto the high speed photodiode was $60 \mu\text{W}$, as well as that the power spectral densities of the first harmonic and the 20th harmonic were adopted in the calculation. It can be seen that the energy fluctuation and the time jitter of the FD1 laser were 0.000063% and 2.18 ps, and that of the SH laser were 0.000011% and 1.56 ps.

4. Conclusion

In conclusion, we have established a theoretical model of the dual-wavelength EO Q-switched laser. The time-varying Q-switched loss, the transmission of OC, the doped concentration of gain medium were all theoretically optimized to achieve dual-wavelength sub-ns lasers with sufficient high energies. Based on theoretical predictions, an EO Q-switched laser combined with an extra-cavity SHG was constructed. When the high-level-voltage of the driving signal was set as 1.4 times as the quarter wave voltage of PC, the $\text{YVO}_4\text{-Nd (1 at. %):YVO}_4$ composite crystal and the OC with a transmission of 70% were used, 1 kHz, sub-ns 1064 nm and 532 nm single-longitudinal-mode pulse lasers were obtained. At a pump energy of 3.7 mJ, the PWs of the 1064 nm and 532 nm lasers were 0.97 ns and 0.61 ns, the SPEs of the two were 0.55 mJ and 0.29 mJ. The beam quality factor, the energy fluctuation and the time jitter of the 1064 nm laser were 1.58, 0.000063% and 2.18 ps; and that of the 532 nm laser were 1.35, 0.000011% and 1.56 ps. This kind of high PRF, sub-ns dual-wavelength lasers were favourable excitation source of high speed high resolution PAM for living animals, and more applications can be found in the fields of outdoor detection and laser precision machining.

Acknowledgments

This work was supported by the National Natural Science Foundation of China (NSFC) (62175135), Fundamental Research Program of Shanxi Province (202103021224025).

References

- [1] Bachmann A, Wyler S, Ruszat R, Casella R, Gasser T and Sulser T 2004 80W high-power KTP laser vaporization of the prostate clinical results after 110 consecutive procedures *Eur. Urol.* **3** 145
- [2] Du P, Geng D, Wang W and Gong M 2015 Laser detection of remote targets applying chaotic pulse position modulation *Opt. Eng.* **54** 114102
- [3] Hintikka M and Kostamovaara J 2017 Experimental investigation into laser ranging with sub-ns laser pulses *IEEE Sens. J.* **18** 1047–53
- [4] Rajesh P, James B and Hang-Ru G 2015 Doubling silicon ablation process efficiency and improving quality using high power high repetition rate green laser with time shift capability *J. Laser Micro Nanoeng.* **10** 134–9
- [5] Pratik P S and Jonathan L 2012 The influence of brightness during laser surface treatment of Si_3N_4 engineering ceramics *Opt. Lasers Eng.* **50** 1746–51
- [6] Zhang H F, Maslov K, Stoica G and Wang L V 2006 Functional photoacoustic microscopy for high-resolution and noninvasive *in vivo* imaging *Nat. Biotechnol.* **24** 848–51
- [7] Yao J J, Wang L, Yang J, Maslov K I, Wong T T W, Li L, Huang C H, Zou J and Wang L V 2015 High speed label-free functional photoacoustic microscopy of mouse brain in action *Nat. Methods* **12** 407–10
- [8] Zhu X et al 2022 Real-time whole-brain imaging of hemodynamics and oxygenation at micro-vessel resolution with ultrafast wide-field photoacoustic microscopy *Light Sci. Appl.* **11** 138
- [9] Liu T, Wei Q, Song W, Burke J, Jiao S and Zhang H 2012 Near-infrared light photoacoustic ophthalmoscopy *Biomed. Opt. Express* **3** 792–9
- [10] Yao J J and Wang L V 2014 Sensitivity of photoacoustic microscopy *Photoacoustics* **2** 87–101
- [11] Qin W, Jin T, Guo H and Xi L 2018 Large field of view optical resolution photoacoustic microscopy *Opt. Express* **26** 4271–8
- [12] Zayhowski J and Dill C 1995 Coupled cavity electro-optically Q-switched Nd:YVO₄ microchip lasers *Opt. Lett.* **20** 716–8
- [13] Zhou Y P, Li X D, Xu H B, Yan R P, Jiang Y G, Fan R W and Chen D Y 2021 High-pulse-energy passively Q-switched sub-nanosecond MOPA laser system operating at kHz level *Opt. Express* **29** 17201–14
- [14] Li T, Zhao S Z, Zhuo Z, Yang K J, Li G Q and Li D C 2009 Pulse-width reduction in a diode-pumped doubly Q-switched $\text{YVO}_4\text{:Nd:YVO}_4$ laser with electro-optic modulator and GaAs saturable absorber *J. Opt. Soc. Am. B* **26** 1146–50
- [15] Turri G, Janssen H P, Cornacchia F, Tonelli M and Bass M 2009 Temperature-dependent stimulated emission cross section in $\text{Nd}^{3+}:\text{YVO}_4$ crystals *J. Opt. Soc. Am. B* **26** 2084–8
- [16] Mukhopadhyay P K, George J, Sharma S K, Ranganathan K and Nathan T P S 2002 Experimental determination of effective stimulated emission cross-section in a diode pumped Nd:YVO₄ micro-laser at 1064nm with various doping concentrations *Opt. Laser Technol.* **34** 357–62
- [17] Chen Y F, Lee L J, Huang T M and Wang C L 1999 Study of high-power diode-end-pumped Nd:YVO₄ laser at 1.34 μm influence of auger upconversion *Opt. Commun.* **163** 198–202
- [18] Rakesh B and Takunori T 2011 >6 MW peak power at 532 nm from passively Q-switched Nd:YAG/Cr⁴⁺:YAG microchip laser *Opt. Express* **19** 19135–41

- [19] Wang L D, Zhang C and Wang L V 2014 Grueneisen relaxation photoacoustic microscopy *Phys. Rev. Lett.* **113** 174301
- [20] Linde D V D 1986 Characterization of the noise in continuously operating mode-locked lasers *Appl. Phys. B* **39** 201–17
- [21] Tang J H and Wang Y C 2006 Spectrum analysis of all parameter noises in repetition rate laser pulse train *Chin. Opt. Lett.* **4** 467–9
- [22] Son J, Rudd J V and Whitaker J F 1991 Noise characterization of a self-mode-locked Ti: sapphire laser *Opt. Lett.* **17** 733–5